Retrieval of Elastodynamic Reflections From Passive Double-Couple Recordings

Hartstra, I. E.; Almagro Vidal, C.; Wapenaar, K.

DOI
10.1002/2017JB015137

Publication date
2018

Document Version
Final published version

Published in
Journal of Geophysical Research: Solid Earth

Journal of Geophysical Research: Solid Earth

RESEARCH ARTICLE
10.1002/2017JB015137

Retrieval of Elastodynamic Reflections From Passive Double-Couple Recordings

I. E. Hartstra[1], C. Almagro Vidal[1], and K. Wapenaar[1]

[1]Department of Geoscience and Engineering, Delft University of Technology, Delft, Netherlands

Key Points:
- We introduce elastodynamic full-field multidimensional deconvolution with an exact kernel and point spread function
- We compare of interferometric methods using synthetic double-couple recordings containing *P-SV* converted waves
- Full-field multidimensional deconvolution involves the most stable inversion and is least affected by artifacts

Correspondence to:
I. E. Hartstra,
i.e.hartstra@tudelft.nl

Citation:
Hartstra, I. E., Almagro Vidal, C., & Wapenaar, K. (2018). Retrieval of elastodynamic reflections from passive double-couple recordings. *Journal of Geophysical Research: Solid Earth*, *123*, 3197–3207. https://doi.org/10.1002/2017JB015137

Received 26 OCT 2017
Accepted 13 MAR 2018
Accepted article online 25 MAR 2018
Published online 26 APR 2018

Abstract Virtual Green's functions obtained by seismic interferometry (SI) can provide valuable reflectivity data that can complement tomographic inversion schemes. However, virtual reflections are affected by illumination irregularities that are typical of earthquake-induced wavefields recorded by the receiver array. As a consequence, irregular source distributions, scattering (in case of suboptimal illumination), and complex source mechanisms can significantly disturb the retrieval of Green's function approximations by conventional SI methods. We introduce SI by full-field multidimensional deconvolution (MDD) for elastodynamic wavefields as an alternative method to obtain body wave Green's functions under those typical circumstances. The advantage of this method compared to other MDD methods is that the kernel of its governing equation is exact. This alternative formulation of the kernel pertains to several advantages: the solution is less sensitive to artifacts and utilizes the free-surface multiples in the data to estimate primary reflections. Moreover, the point spread function of the full-field MDD method corrects more affectively for irregular illumination because it also addresses irregularities caused by scattering inside the medium. In order to compare full-field MDD to existing SI methods, we model synthetic earthquake recordings in a subduction zone setting using an elastodynamic finite-difference scheme with double couples of different orientations and peak frequencies. Our results show that SI by cross correlation suffers most under these circumstances. Higher-quality reflections are obtained by the MDD methods, of which full-field MDD involves the most stable inversion, and its results are least contaminated by artifacts.

1. Introduction

The Earth's lithosphere is continuously affected by a natural prevalent stress field that is primarily driven by the motion of tectonic plates over the relatively ductile asthenosphere (Fowler, 2005). Ultimately, natural earthquakes can be triggered when accumulated stress gets released by the collapse of shear (Aki & Richards, 2002). When estimates of the locations and timings of earthquakes are available, the traveltimes of the induced seismic waves can be used to calculate the propagation velocity of the subsurface structure. Correspondingly, a smooth velocity model of the subsurface is obtained from the tomographic inversion of traveltimes of all earthquake-receiver pairs (Kennett, 1998; Nolet, 2008). The accuracy of tomographic models relies on the quality of earthquake timing estimates, which can pose a challenge.

Claerbout (1968) showed that autocorrelation of the recording of the transmission response by a single receiver yields the estimation of the seismic reflection response as if there were a source at the position of this same receiver. The application of reciprocity theorems (de Hoop, 1995) made it possible to extend this 1-D concept to seismic recordings in higher dimensions (Wapenaar, 2004). Obtaining complete virtual reflection surveys by cross-correlating earthquake body wave recordings is a subclass of seismic interferometry (SI) (Larose et al., 2006; Schuster, 2001; Snieder, 2004; Wapenaar, 2004). The methodology is analogous to surface wave Green's function retrieval (Campillo & Paul, 2003; Sabra et al., 2005), except that body waves instead of surface waves are cross-correlated. SI with body waves can provide valuable complementary information of the subsurface structure. It exploits the scattered field from the earthquake recordings to retrieve reflection surveys analogous to those in exploration geophysics. These virtual reflection surveys obtained with SI can yield impedance contrasts with superior vertical resolution and are independent of earthquake timing. Several approaches to body wave interferometry exist of which the cross-correlation method is the most widely used (Schuster, 2009; Wapenaar & Fokkema, 2006).

Green's functions obtained by cross correlation have a well-defined virtual source location and timing and make effective use of the higher wavenumber content of the seismic wavefield. Therefore, they have

the potential to approximate reflections of the subsurface structure, which can be used to determine valuable parameters such as the depth of a subduction slab or the Moho. In the past, body wave SI by cross correlation has been validated numerically with acoustic models (Draganov et al., 2006) and has found numerous field applications (Boué et al., 2014; Draganov et al., 2007; Lin et al., 2013; Nishida, 2013; Tonegawa et al., 2009; Zhan et al., 2010). However, its sensitivity to inhomogeneous illumination conditions in the recorded wavefield can result in spurious events and inaccurate amplitudes that affect the accuracy of the estimated Green's function. Natural seismic illumination is inherently irregular, due to the uneven spatial distribution of earthquakes and also due to scattering inside the medium and the complex source mechanisms of earthquakes. This renders it unlikely to obtain Green's function estimates that contain accurate reflections with SI by cross correlation on field data.

Several approaches have been proposed that deal with one or more of these limitations. For example, by applying appropriate weighting one can effectively correct for the illumination irregularities that cause artifacts in Green's function estimate (Almagro Vidal et al., 2014; Curtis & Halliday, 2010). Although this approach has proven successful, it is sensitive to the choice of weights. Following a different strategy, Fichtner et al. (2017) proposed a method that exploits the benefits of SI for the purpose of tomographic inversion, by circumventing the requirement to obtain an accurate Green's function between receivers. Instead of inverting for the accurate Green's function, the inverse problem is formulated for the cross-correlation function that is actually obtained by SI, thereby taking its artifacts into account.

SI by multidimensional deconvolution (MDD) methods offer alternatives to cross correlation for obtaining Green's functions from earthquake recordings (van der Neut et al., 2010; Wapenaar, van der Neut, & Ruigrok, 2008). These methods aim to correct for any irregularities in the virtual source radiation by inversion: a deconvolution process that involves all receivers simultaneously, hence the term "multidimensional." Acoustic numerical experiments using an irregular distribution of passive monopole sources showed that MDD yields a more accurate Green's function than cross correlation. Essential in this process is the formulation of the quantity that is inverted: the interferometric point spread function (PSF). The PSF has encoded the spectral information of the virtual source radiation pattern that it aims to balance, such that the spurious events and incorrect amplitudes of the retrieved reflections get minimized.

Almagro Vidal (2017) showed that, for body wave interferometry, two main types of MDD methods can be distinguished by the manner in which they utilize the free-surface multiples from the earthquake recordings and the spectral content of the PSF: ballistic and full-field MDD. Ballistic MDD (Wapenaar, van der Neut, & Ruigrok, 2008) approximates the PSF from the directly incident (ballistic) wavefield to obtain Green's function with free-surface multiples, while full-field MDD uses the full recorded wavefield to construct the PSF to yield Green's function without free-surface multiples (Hartstra et al., 2017). Acoustic numerical experiments using a limited distribution of passive dipole sources with varying radiation patterns showed that full-field MDD yields a more accurate Green's function than cross correlation and ballistic MDD. Ballistic MDD, formulated for decomposed one-way wavefields in elastic media, has been applied to obtain virtual reflections from field data (Nakata et al., 2014). The main challenge of MDD applications is that they require an estimation of the earthquake recordings without free-surface multiples.

For the purpose of obtaining an accurate Green's function from earthquake recordings, we propose elastodynamic full-field MDD as an alternative interferometric method. We conduct numerical experiments in order to compare the quality of Green's functions obtained by cross correlation, ballistic MDD (as well as an approximation of this method), and full-field MDD. These interferometric methods have been validated in previous work with acoustic models using monopole or dipole passive sources. However, the acoustic regime cannot take into account certain characteristics of a typical field setting that could have significant impact on the performance of SI methods. In a field setting, the recorded passive wavefield contains *P* and *S* converted waves generated by earthquake source mechanisms that radiate the seismic energy in a complex and unique manner (Stein & Wysession, 2003). In order to make a realistic comparison, we generate synthetic earthquake recordings by implementing double couples with varying peak frequencies, magnitudes, and orientations in an elastic subduction zone model.

2. Methods

In this section, we present the different SI methods employed for body wave reflection retrieval at the free surface and analyze their validation for elastodynamic scenarios.

2.1. Cross Correlation

There exist several ways to derive the governing equation for the cross-correlation method. Here a distinction can be made between the expression for closed systems (Lobkis & Weaver, 2001) and for open systems (Claerbout, 1968; Derode et al., 2003; Snieder, 2004). We apply SI by cross correlation based on the reciprocity theorem of the correlation type for open systems (de Hoop, 1995) and work with an approximation of the 3-D elastodynamic cross-correlation expression in the frequency domain (equation (80) from Wapenaar & Fokkema, 2006):

$$\Re\left[\hat{R}_{k|j}(\mathbf{x}_A,\mathbf{x}_R,\omega)\right]\langle\hat{S}(\omega)\rangle \propto \int_{\partial\mathbb{D}_S}\hat{V}_k(\mathbf{x}_A,\mathbf{x}_B,\omega)\hat{V}_j^*(\mathbf{x}_R,\mathbf{x}_B,\omega)\mathrm{d}^2\mathbf{x}_B, \tag{1}$$

Note that we use a proportionality symbol, because we adjusted equation (80) from Wapenaar and Fokkema (2006) by neglecting the effects of the imprint of the passive source radiation patterns and possible variations of the medium parameters along the passive sources. We use the symbol R to denote the reflection response Green's function throughout this article. The desired $\hat{R}_{k|j}(\mathbf{x}_A,\mathbf{x}_R,\omega)$ is the k-component of the particle velocity reflection response of the medium with free surface, observed at $\mathbf{x}_A$ due to a virtual j-component traction source at $\mathbf{x}_R$, both at the free surface. ω denotes the angular frequency. The symbol $\Re$ indicates that we obtain the real part of this reflection response, which is multiplied with the average of the earthquakes' power spectra: $\hat{S}(\omega)$. $\hat{V}_k(\mathbf{x}_A,\mathbf{x}_B,\omega)$ is the particle velocity field measured at receiver $\mathbf{x}_A$ due to an earthquake at an unknown position in the subsurface, $\mathbf{x}_B$. Note that superscript * denotes complex conjugation, which implies that the product in the integrand corresponds to cross correlation in the time domain. The integral in the right-hand side of (1) is defined along the earthquake locations $\mathbf{x}_B \in \partial\mathbb{D}_S$ in the subsurface. This integral imposes the requirement on SI by cross correlation that the earthquakes must form a uniform spatial distribution along an arbitrary boundary $\partial\mathbb{D}_S$ in the subsurface. Note that we will apply equation (1) in 2-D, which means that the earthquakes must be distributed along a continuous line boundary $\partial\mathbb{D}_S$. Since in interferometry we assume to have no prior knowledge of the source characteristics, we do not take into account the medium parameters surrounding the source nor the specifics of the source radiation pattern.

2.2. Ballistic MDD

SI by ballistic MDD is based on the reciprocity theorem of the convolution type. Its governing equation for elastodynamic wavefields in 3-D media reads (Wapenaar, van der Neut, & Ruigrok, 2008):

$$\int_{\partial\mathbb{D}_R}\hat{R}_{k|j}(\mathbf{x}_A,\mathbf{x}_R,\omega)\hat{\tau}^o_{j3}(\mathbf{x}_R,\mathbf{x}_B,\omega)\mathrm{d}^2\mathbf{x}_R \approx \hat{V}_k(\mathbf{x}_A,\mathbf{x}_B,\omega) - \hat{V}^o_k(\mathbf{x}_A,\mathbf{x}_B,\omega), \tag{2}$$

where the integral is along a limited array of receivers positioned at $\mathbf{x}_R$ at a horizontal acquisition surface $\partial\mathbb{D}_R$ which we choose to be a free surface. $\hat{V}_k(\mathbf{x}_A,\mathbf{x}_B,\omega)$ and $\hat{V}^o_k(\mathbf{x}_A,\mathbf{x}_B,\omega)$ are the particle velocity recordings at receiver $\mathbf{x}_A \in \partial\mathbb{D}_R$ with and without free-surface multiples, respectively, (the latter indicated by superscript o) due to an earthquake at an unknown position $\mathbf{x}_B$ in the medium. Note that the source properties of the earthquakes do not impose any conditions on the validity of this representation. $\hat{\tau}^o_{j3}(\mathbf{x}_R,\mathbf{x}_B,\omega)$ is the stress field without free-surface multiples measured at receiver $\mathbf{x}_R$ due to the same earthquake at $\mathbf{x}_B$. The integration in the left-hand side involves all the receiver locations along the acquisition surface. Contrary to the explicit equation (1), equation (2) is an implicit relation for $\hat{R}_{k|j}$, where the product within the integral stands for a convolution in the time domain.

In order to solve for the desired reflection response $\hat{R}_{k|j}$, we first approximate the kernel of the equation, $\hat{\tau}^o_{j3}$, by the particle velocity recordings:

$$\hat{\tau}^o_{13}(\mathbf{x}_R,\mathbf{x}_B,\omega) \approx \rho c_S\hat{V}^o_1(\mathbf{x}_R,\mathbf{x}_B,\omega), \tag{3}$$

$$\hat{\tau}^o_{23}(\mathbf{x}_R,\mathbf{x}_B,\omega) \approx \rho c_S\hat{V}^o_2(\mathbf{x}_R,\mathbf{x}_B,\omega), \tag{4}$$

$$\hat{\tau}^o_{33}(\mathbf{x}_R,\mathbf{x}_B,\omega) \approx \rho c_P\hat{V}^o_3(\mathbf{x}_R,\mathbf{x}_B,\omega), \tag{5}$$

whereby we make the pragmatic assumption that the horizontal component is dominated by S waves and the vertical component by P waves. Here c_P and c_S are the averaged P and S velocity values and ρ the density of the medium at the receiver level. The thickness of the layer over which must be averaged to determine these velocities at the receiver level depends on the dominant wavelength of the recordings. Note that the wavefield $\hat{V}^o_j$ includes upgoing direct arrivals and internal multiples from the earthquake recordings but explicitly

excludes any arrivals that interacted with the free surface. Since it is very difficult to remove surface-related multiples from earthquake recordings $\hat{V}_j$, we only use their upgoing direct P and S arrivals to approximate $\hat{V}_j^o$. We refer to these upgoing direct arrivals of earthquake recordings as the "ballistic field," and we denote them with a superscript ^{D}: $\hat{V}_j^o \approx \hat{V}_j^D$. Considering that the downgoing part of the direct arrivals interacted with the free surface, we multiply the direct P wave ($\hat{V}_j^{P,\mathrm{dir}}$) and S wave ($\hat{V}_j^{S,\mathrm{dir}}$) arrivals of $\hat{V}_j$ by a factor of 1/2 in order to select only the upgoing part. The direct wave approximation ($\hat{V}_j^D$) of the $\hat{V}_j^o$ field thus becomes

$$\hat{V}_j^o \approx \hat{V}_j^D = \frac{1}{2}\hat{V}_j^{P,\mathrm{dir}} + \frac{1}{2}\hat{V}_j^{S,\mathrm{dir}}. \tag{6}$$

Note that this is a crude approximation, since elastodynamic conversion at the free surface results in angle-dependent reflection coefficients. A more accurate estimation of upgoing fields could be obtained by applying elastodynamic wavefield decomposition (Nakata et al., 2014; Wapenaar, Slob, & Snieder, 2008). Since our objective is to keep processing to a minimum and to ensure that the methods remain straightforward for field applications, we stick with approximation (6). Introducing the aforementioned approximations (3)–(6) into equation (2) gives

$$\int_{\partial\mathbb{D}_R} \hat{R}_{k|j}(\mathbf{x}_A, \mathbf{x}_R, \omega) w \hat{V}_j^D(\mathbf{x}_R, \mathbf{x}_B, \omega) \mathrm{d}^2\mathbf{x}_R \approx \hat{V}_k(\mathbf{x}_A, \mathbf{x}_B, \omega) - \hat{V}_k^D(\mathbf{x}_A, \mathbf{x}_B, \omega), \tag{7}$$

with weights

$$w = \begin{cases} \rho c_S, & \text{if } j = 1, 2 \\ \rho c_P, & \text{if } j = 3 \end{cases}.$$

Equation (7) forms a Fredholm integral of the first kind (Arfken & Weber, 2005) with a kernel that is approximated by the ballistic field of each respective earthquake recording. We formulate this problem in 2-D ($j = 1, 3$) and employ a matrix notation (Berkhout, 1982)

$$\begin{bmatrix} \hat{\mathbf{R}}_{1|1} & \hat{\mathbf{R}}_{1|3} \\ \hat{\mathbf{R}}_{3|1} & \hat{\mathbf{R}}_{3|3} \end{bmatrix} \begin{bmatrix} \rho c_S \hat{\mathbf{V}}_1^D \\ \rho c_P \hat{\mathbf{V}}_3^D \end{bmatrix} \approx \begin{bmatrix} \hat{\mathbf{V}}_1 - \hat{\mathbf{V}}_1^D \\ \hat{\mathbf{V}}_3 - \hat{\mathbf{V}}_3^D \end{bmatrix}. \tag{8}$$

The field matrices $\hat{\mathbf{V}}_k$ and $\hat{\mathbf{V}}_k^D$, respectively, contain the independent nonoverlapping recordings of earthquakes and their direct arrivals, whereby each row represents a receiver position and each column an earthquake. The reflection responses $\hat{\mathbf{R}}_{k|j}$ are square matrices with rows representing receivers and columns corresponding to independent virtual sources (whose positions coincide with the receivers). The normal form of equation (8) can be obtained by multiplying both sides with the transposed complex conjugated form of the kernel matrix

$$\begin{bmatrix} \hat{\mathbf{R}}_{1|1} & \hat{\mathbf{R}}_{1|3} \\ \hat{\mathbf{R}}_{3|1} & \hat{\mathbf{R}}_{3|3} \end{bmatrix} \rho \begin{bmatrix} c_S^2 \hat{\mathbf{V}}_1^D \hat{\mathbf{V}}_1^{D\dagger} & c_S c_P \hat{\mathbf{V}}_1^D \hat{\mathbf{V}}_3^{D\dagger} \\ c_P c_S \hat{\mathbf{V}}_3^D \hat{\mathbf{V}}_1^{D\dagger} & c_P^2 \hat{\mathbf{V}}_3^D \hat{\mathbf{V}}_3^{D\dagger} \end{bmatrix} \approx \begin{bmatrix} \left(\hat{\mathbf{V}}_1 - \hat{\mathbf{V}}_1^D\right) c_S \hat{\mathbf{V}}_1^{D\dagger} & \left(\hat{\mathbf{V}}_1 - \hat{\mathbf{V}}_1^D\right) c_P \hat{\mathbf{V}}_3^{D\dagger} \\ \left(\hat{\mathbf{V}}_3 - \hat{\mathbf{V}}_3^D\right) c_S \hat{\mathbf{V}}_1^{D\dagger} & \left(\hat{\mathbf{V}}_3 - \hat{\mathbf{V}}_3^D\right) c_P \hat{\mathbf{V}}_3^{D\dagger} \end{bmatrix}, \tag{9}$$

where superscript † indicates transposition and complex conjugation. We can solve for the reflection responses by applying a regularized least squares inversion scheme, yielding the following approximate solution:

$$\begin{bmatrix} \hat{\mathbf{R}}_{1|1} & \hat{\mathbf{R}}_{1|3} \\ \hat{\mathbf{R}}_{3|1} & \hat{\mathbf{R}}_{3|3} \end{bmatrix} \approx \begin{bmatrix} \left(\hat{\mathbf{V}}_1 - \hat{\mathbf{V}}_1^D\right) c_S \hat{\mathbf{V}}_1^{D\dagger} & \left(\hat{\mathbf{V}}_1 - \hat{\mathbf{V}}_1^D\right) c_P \hat{\mathbf{V}}_3^{D\dagger} \\ \left(\hat{\mathbf{V}}_3 - \hat{\mathbf{V}}_3^D\right) c_S \hat{\mathbf{V}}_1^{D\dagger} & \left(\hat{\mathbf{V}}_3 - \hat{\mathbf{V}}_3^D\right) c_P \hat{\mathbf{V}}_3^{D\dagger} \end{bmatrix} \left(\rho \begin{bmatrix} c_S^2 \hat{\mathbf{V}}_1^D \hat{\mathbf{V}}_1^{D\dagger} & c_S c_P \hat{\mathbf{V}}_1^D \hat{\mathbf{V}}_3^{D\dagger} \\ c_P c_S \hat{\mathbf{V}}_3^D \hat{\mathbf{V}}_1^{D\dagger} & c_P^2 \hat{\mathbf{V}}_3^D \hat{\mathbf{V}}_3^{D\dagger} \end{bmatrix} + \epsilon^2 \mathbf{I} \right)^{-1}, \tag{10}$$

where ϵ^2 is the stabilization parameter and $\mathbf{I}$ is the identity matrix (Arfken & Weber, 2005). By including more recordings of independent earthquake events, the extra illumination information they provide can serve to better constrain the estimation of the reflection responses. Note that the right-hand side of equation (10) represents the process of constructing a correlation function (first term in square brackets) that is subsequently "deblurred" by a PSF (second term in square brackets). However, since it is constructed by the inexact kernel of the original equation (7), this PSF will not be exact: it is approximated by the direct arrivals, the ballistic field, of the earthquake recordings.

The ballistic PSF has two disadvantages. The first is caused by the fact that the input wavefield is obtained from the earthquake recordings by a time-windowing procedure, which requires a taper and is user dependent. During its inversion (equation (10)) this will inevitably contaminate the solution. Second, since only direct waves are used to construct it, the PSF will not be able to balance illumination irregularities caused by

scattering inside the medium. Just like SI by cross correlation, ballistic MDD also relies strongly on the natural illumination. Nevertheless, it is capable of correcting for the irregularities in the ballistic field which are due to the effects of nonuniform source distributions and complex varying source mechanisms.

In the case of ambient noise recordings, the direct arrival overlaps with the subsequent arrivals because the source function is too long: this makes it impossible to select the direct arrival by time windowing. Naturally, this does not pose any problems for the application of the cross-correlation method (Lin et al., 2013; Poli et al., 2012; Roux et al., 2005; Stehly et al., 2006). In the case of ballistic MDD, an adaptation is required to deal with the ambient noise scenario: this method involves constructing the PSF by applying time windows after cross correlation (van der Neut et al., 2010; Wapenaar et al., 2011). Acoustic synthetic experiments have shown that the PSF constructed in this way successfully corrects for irregular passive source distributions. The elastodynamic form of this method is formulated with matrix notation in the frequency domain as

$$\begin{bmatrix} \hat{\mathbf{R}}_{1|1} & \hat{\mathbf{R}}_{1|3} \\ \hat{\mathbf{R}}_{3|1} & \hat{\mathbf{R}}_{3|3} \end{bmatrix} \approx \begin{bmatrix} \hat{\mathbf{V}}_1\hat{\mathbf{V}}_1^\dagger - \hat{\mathbf{\Gamma}}_{11} & \hat{\mathbf{V}}_1\hat{\mathbf{V}}_3^\dagger - \hat{\mathbf{\Gamma}}_{13} \\ \hat{\mathbf{V}}_3\hat{\mathbf{V}}_1^\dagger - \hat{\mathbf{\Gamma}}_{31} & \hat{\mathbf{V}}_3\hat{\mathbf{V}}_3^\dagger - \hat{\mathbf{\Gamma}}_{33} \end{bmatrix} \left(\begin{bmatrix} \hat{\mathbf{\Gamma}}_{11} & \hat{\mathbf{\Gamma}}_{13} \\ \hat{\mathbf{\Gamma}}_{31} & \hat{\mathbf{\Gamma}}_{33} \end{bmatrix} + \epsilon^2\mathbf{I} \right)^{-1}, \tag{11}$$

where the virtual ballistic PSF, $\hat{\mathbf{\Gamma}}_{kj}$, contains the virtual source radiation pattern which is selected with time windows around $t = 0$ from the inverse Fourier transform of $\hat{\mathbf{V}}_k\hat{\mathbf{V}}^\dagger{}_j$. The limits of this time window are defined by the virtual direct *P* wave arrival and its time reversal. However, we emphasize that the stability of the solution is very sensitive to the selection of the time window for this PSF, which is particularly difficult to calibrate correctly in the case of field data. Since this method was specifically developed for ambient noise SI (ANSI) applications, we refer to it here as ANSI-MDD.

2.3. Full-Field MDD

SI by full-field MDD is based on the reciprocity theorem of the convolution type. The 3-D elastodynamic form of full-field MDD for two-way wavefields (Hartstra et al., 2017) reads

$$\int_{\partial\mathbb{D}_R} \hat{R}^o_{k|i3}(\mathbf{x}_A, \mathbf{x}_R, \omega)\hat{V}_i(\mathbf{x}_R, \mathbf{x}_B, \omega)\mathrm{d}^2\mathbf{x}_R \approx \hat{V}_k(\mathbf{x}_A, \mathbf{x}_B, \omega) - \hat{V}^o_k(\mathbf{x}_A, \mathbf{x}_B, \omega), \tag{12}$$

where the integral is along a limited array of receivers positioned at $\mathbf{x}_R$ at a horizontal acquisition surface $\partial\mathbb{D}_R$ which we choose to be at the free surface. Like equation (7), this equation presents a Fredholm integral of the first kind but with a kernel, $\hat{V}_i(\mathbf{x}_R, \mathbf{x}_B, \omega)$, that does not require approximations: it is the observed particle velocity recording of an earthquake including free-surface multiples. The solution $\hat{R}^o_{k|i3}(\mathbf{x}_A, \mathbf{x}_R, \omega)$ is the *k*-component particle velocity response at $\mathbf{x}_A$ due to an uniaxial or a simple-shear stress point source, depending on subscript *i*, at position $\mathbf{x}_R$, without free-surface multiples. Note that, because of the different source types, $\hat{R}^o_{k|i3}$ in equation (12) has a different dimension than $\hat{R}_{k|j}$ in equation (2). The right-hand side of equation (12) is exactly the same as in equation (2). Therefore, we apply the same approximation as used there: $\hat{V}^o_k(\mathbf{x}_A, \mathbf{x}_B, \omega)$ is estimated by selecting the direct *P* and *S* arrivals from the earthquake recordings, $\hat{V}_k(\mathbf{x}_A, \mathbf{x}_B, \omega)$, and multiplying both by a factor of 1/2 (this approximation is again denoted as $\hat{V}^D$). The regularized least squares solution of equation (12) using the matrix notation becomes in 2-D

$$\begin{bmatrix} \hat{\mathbf{R}}^o_{1|13} & \hat{\mathbf{R}}^o_{1|33} \\ \hat{\mathbf{R}}^o_{3|13} & \hat{\mathbf{R}}^o_{3|33} \end{bmatrix} \approx \begin{bmatrix} (\hat{\mathbf{V}}_1 - \hat{\mathbf{V}}^D_1)\hat{\mathbf{V}}_1^\dagger & (\hat{\mathbf{V}}_1 - \hat{\mathbf{V}}^D_1)\hat{\mathbf{V}}_3^\dagger \\ (\hat{\mathbf{V}}_3 - \hat{\mathbf{V}}^D_3)\hat{\mathbf{V}}_1^\dagger & (\hat{\mathbf{V}}_3 - \hat{\mathbf{V}}^D_3)\hat{\mathbf{V}}_3^\dagger \end{bmatrix} \left(\begin{bmatrix} \hat{\mathbf{V}}_1\hat{\mathbf{V}}_1^\dagger & \hat{\mathbf{V}}_1\hat{\mathbf{V}}_3^\dagger \\ \hat{\mathbf{V}}_3\hat{\mathbf{V}}_1^\dagger & \hat{\mathbf{V}}_3\hat{\mathbf{V}}_3^\dagger \end{bmatrix} + \epsilon^2\mathbf{I} \right)^{-1}. \tag{13}$$

Different from the ballistic PSF of equation (10), the full-field PSF (i.e., the inverted matrix on the right-hand side) does not require approximations nor is affected by time-windowing procedures. However, its main advantage over the ballistic PSF is that it contains the maximum spectral information as provided by the full earthquake recording. Therefore, full-field MDD is less dependent on obtaining the required spectral information from the ballistic field of the earthquakes, since it additionally exploits the spectral information contained in the earthquake's scattering coda and thus also corrects for illumination irregularities caused by scattering (Almagro Vidal, 2017; Hartstra et al., 2017).

3. Numerical Experiments

We analyze the performance of the different SI methods using an elastodynamic finite-difference code to simulate independent, nonoverlapping earthquake recordings in 2-D media (Thorbecke & Draganov, 2011). Figure 1 depicts our model design, inspired by the Cascadia subduction zone (Chen et al., 2015).

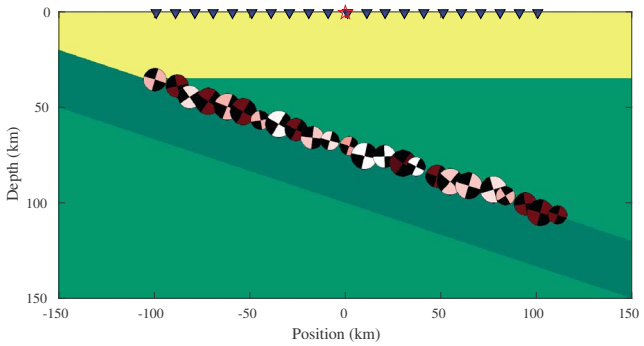

Figure 1. Elastic subduction zone model based on results from Chen et al. (2015): Yellow indicates the crust, green the mantle, and dark green the subduction slab. Sources are indicated by beach balls (see Figure 2) and receivers as blue inverted triangles, and the virtual source position we show results for is indicated by the red star.

The lithospheric crust has *P* and *S* wave velocities of 6 and 3.5 km/s, respectively, and the Moho is at a depth of 35 km. The mantle material below has *P* and *S* wave velocities of 8 and 4 km/s, and the subducting oceanic slab has velocities of 8.5 and 4.25 km/s, respectively. The densities of the crust, mantle, and slab are 2,700, 3,000, and 3,500 kg/m^3, respectively.

In order to simulate recordings of realistic earthquake sources, we implement shear stress sources with a typical double-couple radiation pattern. Besides some exceptions, for example, volcanic eruptions, earthquakes are generally triggered by a release of accumulated shear stress, accommodated by the sudden movement of rock masses along a fault plane. The geometry of the fault and the petrophysical parameters of the surrounding rock masses determines the initial radiation characteristics of the source mechanism of the earthquake, such as magnitude, frequency content, and the directional radiation of seismic waves. The fault-slip motion radiates both *P* and *S* waves in a complex manner and can be approximated using the double-couple model (Aki & Richards, 2002; Stein & Wysession, 2003). The double-couple model describes the radiation of *P* and *S* waves whose quadrupole radiation patterns are rotated 45° with respect to each other (Figure 2). We distribute a total number of 70 shear stress sources irregularly along the top of the subducting slab to simulate the effect of stress release induced by tectonic forces. The source mechanisms vary randomly in peak frequency (between 0.4 and 1 Hz), orientation (between 0 and 360°), and an amplitude factor (3–5). We use a Ricker wavelet as source function. The band-limiting properties of this particular source function prevent aliasing of the synthetic wavefields, which can be achieved for the case of real data by applying an appropriate band-pass filter.

3.1. Processing

Ballistic and full-field MDD require an estimation of the elastodynamic $\hat{V}^o$ field that defines the earthquake recording without free-surface multiples. We obtain an approximation of the elastodynamic $\hat{V}^o$ response

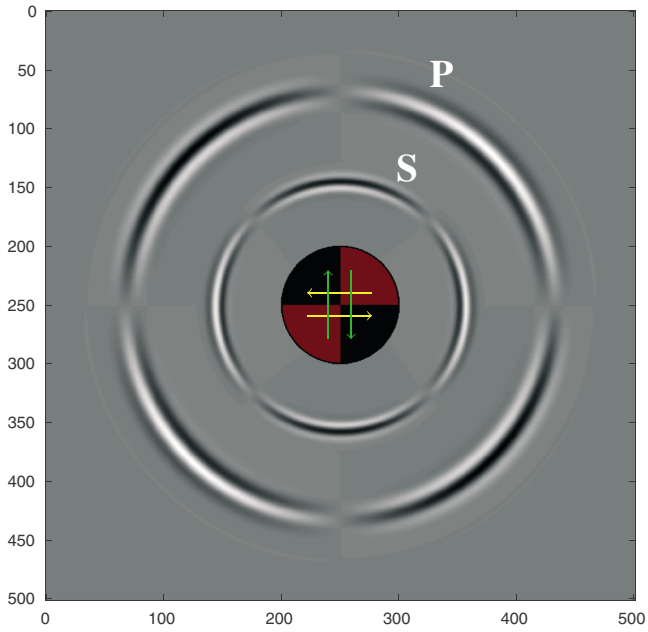

Figure 2. Two-dimensional snapshot of *P* and *S* wave radiation from the double-couple model we implemented to obtain the synthetic recordings. The horizontal and vertical axes indicate the number of grid cells which have a size of 200 m. The yellow and green arrows indicate the two possible fault-slip motions which can both generate this specific elastodynamic radiation pattern. The beach ball in the middle is the symbol we use in Figure 1 to denote the position, orientation, and peak frequency of the double couples. We use black to denote compression, which has positive amplitude. Dilatation, which has negative amplitude, is denoted with a varying color to indicate the peak frequency of the source wavelet, which varies from dark red (0.4 Hz) to white (1 Hz).

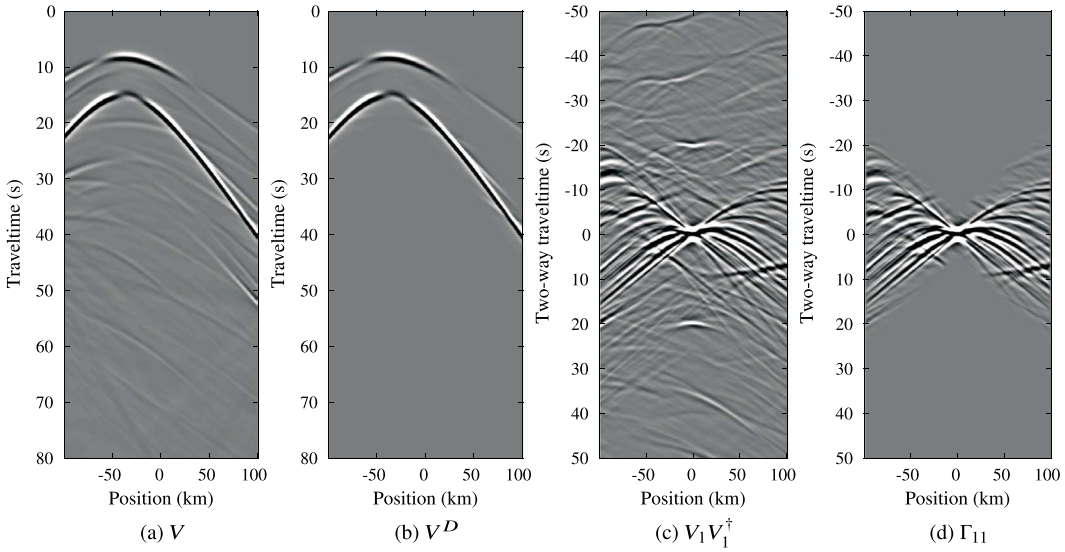

Figure 3. Seismic interferometry processing. (a) Example of one of the independent synthetic earthquake recordings. (b) The V^D approximation: the V^o field is estimated by selecting the direct *P* and *S* wave, which are multiplied by 1/2, of the recording in Figure 3a. (c) Cross-correlation function forms the input for ambient noise Seismic interferometry-multidimensional deconvolution. (d) The point spread function of equation (11) selected by a tapered time window from the cross-correlation function shown in Figure 3c.

of each independent earthquake recording in the time domain (Figure 3a) by selecting one half of the direct *P* and *S* waves with a tapered time window (Figure 3b). This wavefield is the time domain representation of $\hat{V}^D$, which serves to approximate the $\hat{V}^o$ field (equation (6)). For SI by cross correlation, approximate Green's functions are obtained by a straightforward cross correlation of the earthquake recordings. In turn, ANSI-MDD requires the resulting cross-correlation functions as input (see Figure 3c). In order to construct the PSF in equation (11), the virtual source functions are extracted from the cross-correlation functions by applying a time symmetric tapered time window that only selects the part of the cross-correlation function between, and including, the causal and acausal virtual direct *P* wave arrival. We do not select the virtual direct *S* wave arrival because this would inevitably include parts of virtual primary reflections in the PSF, which would increase the appearance of artifacts in the final result. Figure 3d shows an example of a PSF that was obtained by applying the tapered time window to the cross-correlation function shown in Figure 3c.

3.2. Results

For 2-D media, each SI method produces four different elastodynamic responses. Here we analyze only two types of elastodynamic responses per SI method: the vertical and horizontal particle velocity responses due to a horizontally oriented point source (positioned at the middle receiver). Note that full-field MDD retrieves virtual responses to a simple-shear point source (quadrupole) oriented with respect to the acquisition surface without free-surface multiples, while the other three methods retrieve virtual responses to a horizontal force point source (dipole) with free-surface multiples.

Figure 4c shows the vertical particle velocity reflection response, and Figure 4h shows the horizontal particle velocity response to a shear stress source at the middle receiver, serving as reference responses to assess the quality of the reflection retrieval of each method. In these reference responses, the *PP*, *SS*, and *PS*/*SP* reflections of the Moho are identifiable (indicated by yellow arrows). As for the reflections from the top and bottom of the subduction slab, we only focus on their respective *PP*, *SS*, and *PS* converted reflections (top reflections are indicated by green and bottom reflections by blue arrows).

The results from cross correlation (equation (1)) are shown in Figures 4a and 4f. In comparing these results to their corresponding reference responses, most of the arrivals are correctly retrieved, although we do observe a lower-frequency content and a significant number of artifacts. In spite of this, some relevant features can still be distinguished, for example, the near-offset amplitude versus offset (AVO) behavior of the Moho's *PP* and *PS* reflections in Figure 4a is accurately reconstructed, as well as the Moho's *SS* reflection in Figure 4f.

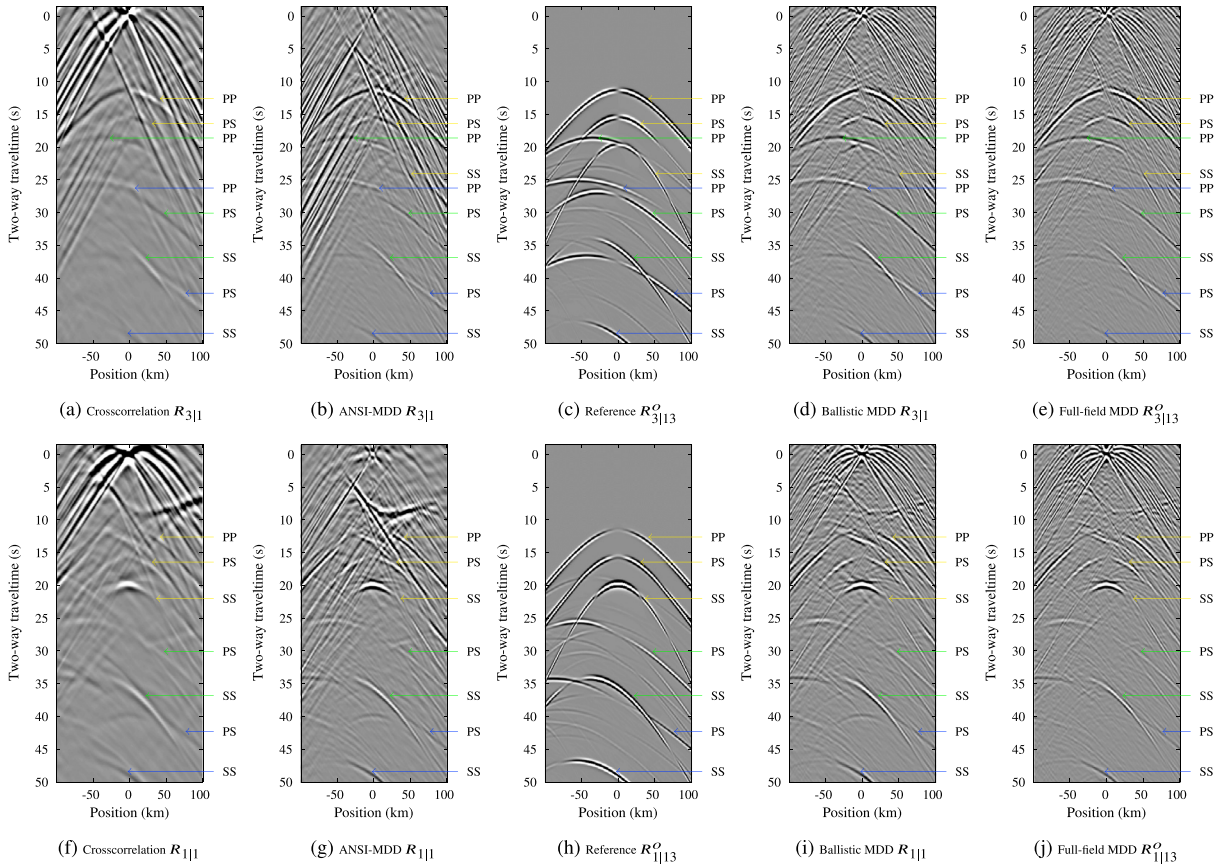

Figure 4. Virtual reflection responses obtained with the seismic interferometry methods from recordings of double couples. (a) Vertical particle velocity response to a horizontal dipole by cross correlation. (b) Idem as (a) by ambient noise seismic interferometry-multidimensional deconvolution (MDD). (c) Reference vertical particle velocity reflection response to a shear stress source. (d) Idem as (a) by ballistic MDD. (e) Vertical particle velocity response to a shear stress source by full-field MDD. (f)–(j) Similar to (a)–(e) but for horizontal particle velocity.

Figures 4b and 4g correspond to the results obtained by ANSI-MDD. The retrieval of the reflections has improved when compared to the corresponding cross-correlation results (Figures 4a and 4f). However, the inversion proved unstable: strong artifacts still partially obscure the reflections, while a stabilization parameter of 80% of the maximum absolute value of the corresponding PSF was required. We also observed that the results were highly sensitive to the time limits of the PSF selection window: we needed to manually adjust the limits of the time window in order to obtain acceptable results.

For the other two methods, ballistic and full-field MDD, we employ equations (10) and (13), respectively, to obtain their reflection responses. The results of ballistic (Figures 4d and 4i) and full-field MDD (Figures 4e and 4j) are significantly better resolved and feature less artifacts than the results obtained by cross correlation and ANSI-MDD. These figures show that all events visible in the reference responses are also visible in both the MDD results, with the same high resolution. Most of the AVO features are accurately resolved, such as the *PP* Moho reflection in Figures 4d and 4e and the *SS* Moho reflection in Figures 4i and 4j. Both methods required little stabilization: 4% for ballistic MDD and 3% for full-field MDD.

The ballistic MDD equation (10) and the full-field MDD equation (13) contain the $\hat{\mathbf{V}}^o$ field that we estimate using the direct *P* and *S* arrival: $\hat{\mathbf{V}}^D$ (see Figure 3b). In order to better understand the sensitivity of the ballistic and full-field MDD methods to the accuracy of the $\hat{\mathbf{V}}^D$ approximation, we show additional solutions in Figure 5 for which we only used the direct *P* wave for $\hat{\mathbf{V}}^D$. Figures 5a and 5b show that excluding the direct *S* wave from $\hat{\mathbf{V}}^D$ does not strongly affect the result: only the slab reflections are more difficult to discern in Figure 5b. However, in case of the horizontal particle velocity response, the Moho reflections also become less clear (Figure 5g). The effect of omitting the direct *S* wave from $\hat{\mathbf{V}}^D$ is much more severe in the case of ballistic MDD: the results shown in Figures 5e and 5j are both seriously contaminated by artifacts and do not resemble the results in Figures 5d and 5i.

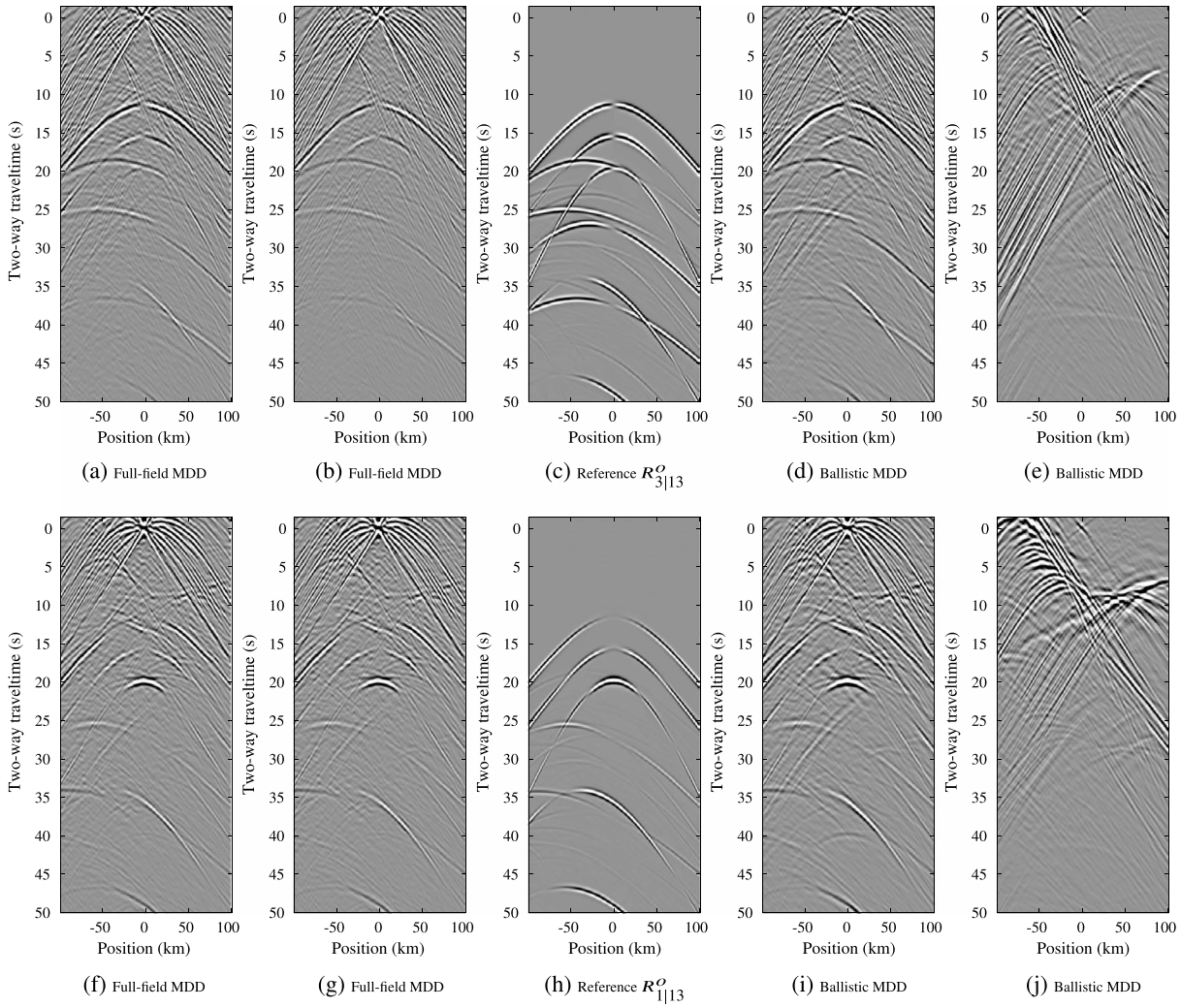

Figure 5. Ballistic and full-field MDD results using two different $\hat{V}^D$ approximations to estimate the $\hat{V}^o$ field. (a) Full-field MDD result $R^o_{3|13}$ using $\hat{V}^D = \frac{1}{2}\hat{V}^{P,\mathrm{dir}} + \frac{1}{2}\hat{V}^{S,\mathrm{dir}}$. (b) Full-field MDD result $R^o_{3|13}$ using $\hat{V}^D = \frac{1}{2}\hat{V}^{P,\mathrm{dir}}$. (c) Reference vertical particle velocity reflection response to a shear stress source. (d) Ballistic MDD result $R_{3|1}$ using $\hat{V}^D = \frac{1}{2}\hat{V}^{P,\mathrm{dir}} + \frac{1}{2}\hat{V}^{S,\mathrm{dir}}$. (e) Ballistic MDD result $R_{3|1}$ using $\hat{V}^D = \frac{1}{2}\hat{V}^{P,\mathrm{dir}}$. (f)–(j) Similar to (a)–(e) but for horizontal particle velocity.

4. Discussion

The cross-correlation results in Figures 4a and 4f have a lower quality than those of full-field and ballistic MDD. This can be explained by the fact that the cross-correlation equation (1) is designed for smoothly distributed passive sources with constant isotropic radiation patterns. Because of this, it cannot be expected to adequately correct for the highly anisotropic radiation patterns of double couples with varying source characteristics (Figure 2). Moreover, equation (1) shows that cross correlation will yield a reflection response estimate that is convolved with the average of the earthquakes' spectra, *S*. Therefore, the resolution of the reflection response is largely determined by the peak frequencies of the earthquakes' source functions. On the other hand, the deconvolution process of the MDD methods results in a flattening of the spectrum of the final solution. Hence, these methods exploit the full frequency band as provided by the natural illumination.

Figures 4b and 4g show that the elastodynamic form of ANSI-MDD primarily improves the resolution of the cross-correlation results. However, the use of a very high stabilization parameter of 80% did not prevent the reflections to become partially obscured by inversion-related artifacts. This shows that the inversion is unstable. Another disadvantage of the ANSI-MDD method is that the solution is highly sensitive to the user-dependent process of selecting the PSF with a time window from the cross-correlation functions. This will particularly cause problems in the case of field data, when it is more challenging to adjust the limits

of the PSF selection window to obtain optimal results. Hence, for transient-source responses we do not recommend to use the ANSI-MDD method, but for ambient noise it is the only MDD method and hence worth to be further investigated.

The application of full-field and ballistic MDD resulted in more stable and accurate estimates of virtual body wave reflections. However, Figures 5e and 5j show that when the direct *S* wave, $\hat{V}_j^{S,\mathrm{dir}}$, is omitted from the $\hat{\mathbf{V}}^D$ approximation, the ballistic MDD results become severely contaminated by artifacts. The full-field MDD results are considerably less affected by this (Figures 5b and 5g). The fact that the PSF of ballistic MDD is constructed by the $\hat{\mathbf{V}}^D$ field (see equation (10) could explain its higher sensitivity to the accuracy of the $\hat{\mathbf{V}}^D$ approximation. By omitting $\hat{V}_j^{S,\mathrm{dir}}$, the ballistic PSF loses its ability to correct for irregularities in the illumination provided by the directly incident *S* wavefield. Moreover, this omission has as a result that the free-surface multiples in the earthquake recordings that are initiated by direct *S* waves cannot be explained and therefore generate artifacts. On the other hand, changes in this approximation have no effect on the PSF of full-field MDD since it is constructed by the observed data (equation (13)). This implies that in cases where it is too challenging to extract the direct *S* wave from field data recordings, it suffices to use only the direct *P* wave for the full-field MDD method to obtain a stable result.

The elastodynamic reflections we estimate with either full-field or ballistic MDD can be used directly to estimate *P* and *S* wave velocities or relevant subsurface structures such as the depth of a subducting slab. The accuracy of the AVO reconstruction we observe in the MDD results indicates that it may be possible to perform an elastodynamic AVO analysis on virtual body wave reflections in order to determine valuable petrophysical parameters such as the presence of partial melts or water. However, this would require full illumination conditions and proper spatial sampling of the recordings. Furthermore, these virtual reflections are a useful input for a myriad of tomographic and full waveform inversion schemes, especially considering that MDD methods do not require any knowledge of earthquake source mechanisms, timings, nor locations. Another possible application would be to use the complete virtual seismic surveys as input for exploration imaging techniques. These operations can yield a complete image of the subsurface with maximum vertical resolution and can additionally minimize the effect of interferometric artifacts.

5. Conclusion

We applied four different SI methods to synthetic particle velocity responses of double couples distributed throughout a 2-D elastic subduction zone model. When compared to cross correlation and the approximated form of ballistic MDD (ANSI-MDD), our results indicate that both the full-field and ballistic MDD methods provide more accurate and stable solutions with the least number of artifacts under these circumstances. Essential characteristics of the retrieved reflections, such as the arrival time and AVO behavior, resembled those of the reference responses. Moreover, further analysis revealed that the full-field MDD method is less sensitive to the required estimation of earthquake recordings without free-surface multiples (V^o) than ballistic MDD.

Acknowledgments
The synthetic earthquake recordings and the `Matlab` script with the implementation of elastodynamic full-field MDD can be downloaded with the following link: https://figshare.com/s/da9ed87489352fe35115. We express our gratitude to Jan Thorbecke for his finite-difference code `fdelmodc` (source code and manual can be found on https://janth.home.xs4all.nl) that we used to produce the synthetic earthquake recordings. We thank Joost van der Neut for the insightful discussions. Finally, we are grateful to two anonymous reviewers for their constructive comments that helped to improve the quality of this manuscript.

References

Aki, K., & Richards, P. G. (2002). *Quantative seismology* (2nd ed., pp. 700). Sausalito, California: University Science Books.
Almagro Vidal, C. (2017). Passive seismic interferometry for reflection imaging and monitoring (PhD thesis). Delft University of Technology.
Almagro Vidal, C., Draganov, D., van der Neut, J., Drijkoningen, G., & Wapenaar, K. (2014). Retrieval of reflections from ambient noise using illumination diagnosis. *Geophysical Journal International*, *198*(3), 1572–1584.
Arfken, G. B., & Weber, H. J. (2005). *Mathematical methods for physicists* (6th ed., pp. 1023–1024). New York: Elsevier.
Berkhout, A. J. (1982). *Seismic migration: Imaging of acoustic energy by wave field extrapolation*. Amsterdam: Elsevier.
Boué, P., Poli, P., Campillo, M., & Roux, P. (2014). Reverberations, coda waves and ambient noise: Correlations at the global scale and retrieval of the deep phases. *Earth and Planetary Science Letters*, *391*, 137–145.
Campillo, M., & Paul, A. (2003). Long-range correlations in the diffuse seismic coda. *Science*, *299*, 1615–1618.
Chen, C., Zhao, D., & Wu, S. (2015). Tomographic imaging of the Cascadia subduction zone: Constraints on the Juan de Fuca slab. *Tectonophysics*, *647*, 73–88.
Claerbout, J. F. (1968). Synthesis of a layered medium from its acoustic transmission response. *Geophysics*, *33*(2), 264–269.
Curtis, A., & Halliday, D. (2010). Directional balancing for seismic and general wavefield interferometry. *Geophysics*, *75*(1), SA1–SA14.
de Hoop, A. T. (1995). *Handbook of radiation and scattering of waves* (1st ed.)., pp. pp. 1085. London: Academic Press.
Derode, A., Larose, E., Tanter, M., De Rosny, J., Tourin, A., Campillo, M., & Fink, M. (2003). Recovering the Green's function from field-field correlations in an open scattering medium (L). *The Journal of the Acoustical Society of America*, *113*(6), 2973–2976.
Draganov, D., Wapenaar, K., & Thorbecke, J. (2006). Seismic interferometry: Reconstructing the Earth's reflection response. *Geophysics*, *71*(4), SI61–SI70.
Draganov, D., Wapenaar, K., Mulder, W., Singer, J., & Verdel, A. (2007). Retrieval of reflections from seismic background-noise measurements. *Geophysical Research Letters*, *34*, L04305. https://doi.org/10.1029/2006GL028735

Fichtner, A., Stehly, L., Ermert, L., & Boehm, C. (2017). Generalized interferometry—I: Theory for interstation correlations. *Geophysical Journal International*, *208*(2), 603–638.
Fowler, C. M. R. (2005). *The solid Earth: An introduction to global geophysics* (2nd ed., 685 pp.). Cambridge, UK: Cambridge University Press.
Hartstra, I. E., Almagro Vidal, C., & Wapenaar, K. (2017). Full-field multidimensional deconvolution to retrieve body-wave reflections from sparse passive sources. *Geophysical Journal International*, *210*(2), 609–620.
Kennett, B. L. N. (1998). *Seismic wave propagation and seismic tomography*. Canberra, Australia: Research School of Earth Sciences, Australian National University.
Larose, E., Margerin, L., van Tiggelen, B., Campillo, M., Shapiro, M., Paul, A., et al. (2006). Correlation of random wavefields: An interdisciplinary review. *Geophysics*, *71*, SI11–SI21.
Lin, F.-C., Tsai, V., Schmandt, B., Duputel, Z., & Zhan, Z. (2013). Extracting seismic core phases with array interferometry. *Geophysical Research Letters*, *40*, 4609–4613. https://doi.org/10.1002/grl.50907
Lobkis, O. I., & Weaver, R. L. (2001). On the emergence of the Green's function in the correlations of a diffuse field. *The Journal of the Acoustical Society of America*, *110*(6), 3011–3017.
Nakata, N., Snieder, R., & Behm, M. (2014). Body-wave interferometry using regional earthquakes with multidimensional deconvolution after wavefield decomposition at free surface. *Geophysical Journal International*, *199*(2), 1125–1137.
Nishida, K. (2013). Global propagation of body waves revealed by cross-correlation analysis of seismic hum. *Geophysical Research Letters*, *40*, 1691–1696. https://doi.org/10.1002/grl.50269
Nolet, G. (2008). *A Breviary of seismic tomography: Imaging the interior of the Earth and Sun*. (pp. 343). Cambridge: Cambridge University Press.
Poli, P., Pedersen, H. A., & Campillo, M. (2012). Emergence of body waves from cross-correlation of short period seismic noise. *Geophysical Journal International*, *188*(2), 549–558.
Roux, P., Sabra, K. G., Gerstoft, P., & Kuperman, W. A. (2005). P-waves from cross-correlation of seismic noise. *Geophysical Research Letters*, *32*, L19303. https://doi.org/10.1029/2005GL023803
Sabra, K. G., Gerstoft, P., Roux, P., Kuperman, W. A., & Fehler, M. C. (2005). Surface wave tomography from microseisms in Southern California. *Geophysical Research Letters*, *32*, L14311. https://doi.org/10.1029/2005GL023155
Schuster, G. T. (2001). Theory of daylight/interferometric imaging-tutorial. In *63rd EAGE Conference & Exhibition*. Amsterdam, The Netherlands.
Schuster, G. T. (2009). *Seismic interferometry* (1st ed.). Cambridge: Cambridge University Press.
Snieder, R. (2004). Extracting the Green's function from the correlation of coda waves: A derivation based on stationary phase. *Physical Review E*, *69*(4), 46610.
Stehly, L., Campillo, M., & Shapiro, N. (2006). A study of the seismic noise from its long-range correlation properties. *Journal of Geophysical Research*, *111*, B10306. https://doi.org/10.1029/2005JB004237
Stein, S., & Wysession, M. (2003). *An introduction to seismology, earthquakes, and earth structure* (pp. 512). Boston, MA: Blackwell Publishing.
Thorbecke, J. W., & Draganov, D. (2011). Finite-difference modeling experiments for seismic interferometry. *Geophysics*, *76*, H1–H18.
Tonegawa, T., Nishida, K., Watanabe, T., & Shiomi, K. (2009). Seismic interferometry of teleseismic S-wave coda for retrieval of body waves: An application to the Philippine sea slab underneath the Japanese Islands. *Geophysical Journal International*, *178*, 1574–1586.
van der Neut, J., Ruigrok, E., Draganov, D., & Wapenaar, K. (2010). Retrieving the earth's reflection response by multi-dimensional deconvolution of ambient seismic noise. In *72nd EAGE Conference and Exhibition Incorporating SPE EUROPEC* (P406). Barcelona, Spain.
Wapenaar, K. (2004). Retrieving the elastodynamic Green's function of an arbitrary inhomogeneous medium by cross correlation. *Physical Review Letters*, *93*(25), 254301.
Wapenaar, K., & Fokkema, J. (2006). Green's function representations for seismic interferometry. *Geophysics*, *71*, SI33–SI46.
Wapenaar, K., van der Neut, J., & Ruigrok, E. (2008). Passive seismic interferometry by multidimensional deconvolution. *Geophysics*, *73*(6), A51–A56.
Wapenaar, K., Slob, E., & Snieder, R. (2008). Seismic and electromagnetic controlled-source interferometry in dissipative media. *Geophysical Prospecting*, *56*(3), 419–434.
Wapenaar, K., van der Neut, J., Ruigrok, E., Draganov, D., Hunziker, J., Slob, E., et al. (2011). Seismic interferometry by cross correlation and by multidimensional deconvolution: A systematic comparison. *Geophysical Journal International*, *185*, 1335–1364.
Zhan, Z., Ni, S., Helmberger, D. V., & Clayton, R. W. (2010). Retrieval of Moho-reflected shear wave arrivals from ambient seismic noise. *Geophysical Journal International*, *182*(1), 408–420.